Solar Energy Materials and Solar Cells 186 (2018) 154–164

Contents lists available at ScienceDirect

Solar Energy Materials and Solar Cells

journal homepage: www.elsevier.com/locate/solmat

Broadband antireflective coating stack based on mesoporous silica by acid-catalyzed sol-gel method for concentrated photovoltaic application

Cecilia Agustín-Sáenz[a,*], José Ángel Sánchez-García[a], Maider Machado[a], Marta Brizuela[a], Oihana Zubillaga[a], Agnieszka Tercjak[b]

[a] TECNALIA (Energy and Environment Division) – Parque Científico y Tecnológico de Gipuzkoa, Mikeletegi Pasealekua 2, Donostia-San Sebastián, Spain
[b] Group 'Materials + Technologies' (GMT), Department of Chemical and Environmental Engineering, Faculty of Engineering, Gipuzkoa, University of the Basque Country (UPV/EHU), Plaza Europa 1, 20018 Donostia-San Sebastián, Spain

ARTICLE INFO

Keywords:
Antireflection
Broadband
Silica
Porous coating
Acid-catalyzed
Sol-gel

ABSTRACT

Silica multi-layer stacks have been designed with the aim to provide broadband antireflective (AR) properties for glass components in concentrated photovoltaic (CPV) application. Silica porous coatings were grown by combining acid-catalyzed sol-gel route and evaporation induced self-assembly (EISA) method with four types of organic/inorganic systems. Sols were prepared using tetraethylorthosilicate (TEOS) as inorganic precursor assembled with two di-block copolymers, one tri-block copolymer and one cationic surfactant as organic templates. Optical properties were characterized by ellipsometry and spectrophotometry while the material structure was analyzed by environmental ellipsometric porosimetry (EEP) and atomic force microscopy (AFM). The concentration of inorganic and organic phases was optimized and a broadband AR bi-layer stack was obtained providing a 7.2% (under the reference AM1.5 solar spectral irradiance) increase in transmittance over bare glass in the wavelength range 300–2000 nm when coated on both sides.

1. Introduction

Glass is extensively used in optical and optoelectronic applications such as lenses, screens, substrates for photodetectors, sensors and solar cells assemblies, due to its high optical transmission in a wide wavelength range of the solar spectrum, as well as its high thermal and mechanical stability and relatively low cost. These features justify its use in assembly systems whose application implies exposure to harsh environmental conditions (such as heat, ultraviolet radiation and corrosive media), and needs protection and insulation such as photovoltaic modules [1–3].

Particularly, concentrated photovoltaic (CPV) technology has the potential of becoming the large-scale generation of clean-renewable energy with competitive costs [4]. This technology is based on expensive high efficiency multi-junction III-V solar cells that can currently yield up to ~ 46% conversion efficiency [5] at cell level and 38.9% at module level [5,6], operating at light concentration levels up to 1000× thanks to refractive or reflective cost-effective optical elements, which permit to reduce cell area. The III-V multijunction solar cells are active in a large part of the solar spectrum, and therefore, in order to harvest the full potential of the cells, the module design needs to optimize the optical transmission over the broad wavelength range of 300–2000 nm (broadband performance). An efficient and inexpensive optical design partly compensates the higher cost of multi-junction III–V solar cells [7].

Float glass with low iron content is commonly used for module protection to enhance radiation transmission towards solar cells [2]. However, although this glass exhibits high transparency, Fresnel reflection losses up to 8% [2] are produced at the interface, due to the difference between the refractive indexes of glass and the surrounding medium, generally air.

Antireflection effect between two media with different refractive indexes can be achieved by several approaches such as surface texturing [8,9], interference-type layer stacks by destructive interference of light reflected at different interfaces [10] and multi-layer stacks with graded refractive index structure (GRIN) [1]. Total reflection of the system can be minimized by adjusting the refractive index and thickness of each layer. For a GRIN structure system, depending on the application, antireflective (AR) multi-layer stack may consist of a single layer covering a narrow spectral bandwidth or multiple layers permitting to achieve a broadband optical performance [1].

The required value of refractive index of some the layers partaking in a AR multi-layer stack with GRIN structure needs to be very low and bulk materials cannot meet this criterion. An alternative way is based

* Correspondence to: Mikeletegi Pasealekua 2, 20009 Donostia-San Sebastián, Spain.
E-mail address: cecilia.agustin@tecnalia.com (C. Agustín-Sáenz).

https://doi.org/10.1016/j.solmat.2018.06.040
Received 2 February 2018; Received in revised form 21 June 2018; Accepted 22 June 2018
Available online 30 June 2018

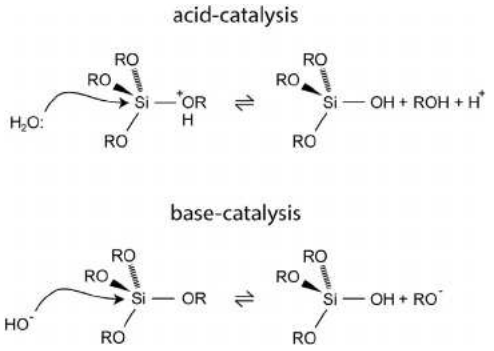

Fig. 1. Hydrolysis of monomeric alkoxysilane under acidic and basic conditions.

on the introduction of voids into the coating materials. Most studies regarding AR coatings following this strategy are based on porous SiO_2 material [11–35]. Moreover, sol-gel method is one of the most attractive processes, offering a precise control of microstructure of the fabricated material by governing features such as volume and size of pores, the surface area and the homogeneity of the coating materials [36,37]. The structure and porosity of the fabricated coating material depend on the relative rates of the hydrolysis and condensation reactions [38] of the sol-gel precursors, and the pH has a crucial influence as well [39,40]. When the hydrolysis reaction of monomeric alkoxysilanes is approached under acidic conditions (see Fig. 1), the alkoxide group is protonated in a first step and electron density is withdrawn from silicon making it more electrophilic and susceptible to water attack [41]. Under basic conditions (see Fig. 1), the water dissociation takes place producing nucleophilic hydroxyl anions, which react with silicon. Successive hydrolysis steps get progressively slower under acidic conditions and faster under basic conditions [42,43] provoking a remarkable difference in the obtained sol and therefore in the structure of the coating material. In basic conditions, small and highly branched agglomerates form a colloidal sol and the coating presents a particulate and porous structure [44] with weak bindings between particles and poor abrasion resistance. In acidic conditions, sol results in chain-like structure and the formed coating is a network-like dense material [38,44] with strong adherence to the substrate and high mechanical properties. In order to obtain porous materials by acid-catalyzed synthesis route, evaporation induced self-assembly method (EISA) was first reported by Asefa et al. [45] and Brinker et al. [46]. Since then the combination of various sol-gel precursors (such as Si, Ti, Zr alkoxides) and various surfactants (anionic, cationic, amphiphilic block copolymer surfactants) has permitted to obtain a large number of mesostructures with pore dimension range from 2 to 20 nm [47]. Trough the preparation of an acid-catalyzed sol containing an inorganic precursor and a surfactant in alcohol medium, the surfactant form micelles that act as structure directing agent (SDA). During the sol to gel transition, the self-assembly of surfactant micelles leads to the creation of an organized texture acting as a template for the inorganic network growth. After elimination of surfactant by calcination, a film with mesoporous structure is obtained.

Although porous silica by sol-gel process has been widely used as AR coatings only in a few occasions has been reported for CPV technology, in which antireflection is required in a broadband range of the solar spectrum in order to cover the range of the multijunction cells operation. Most of the reported research work is focused on the design of mono-layer materials and studies their optical properties only in narrow wavelength band reporting transmission value at a single wavelength. The majority of these studies are based on glass dipping in sols prepared with tetraethyl orthosilicate (TEOS) [13–15,23,25,29,32–35,48–51] and mixture of TEOS and methyl triethoxysilane (MTES) [18–22,24,26,27,31], or even in commercial colloidal silica solution [11,12]. In this research field, Liu et al. [23] have worked with base-catalyzed sol-gel synthesis, which allowed to reach low refractive index equal to 1.22 (estimated from Fresnel equation) similar to the one obtained by Li et al. (experimental at 550 nm) [29], who used the silica coating as part of a multi-layer stack with ZnO_2 reaching high transmittance values (96.1% in the range 300–1200 nm). Some research [30–33,50] have combined base and acid-catalyzed conditions of sol-gel synthesis in order to reach a tradeoff between optical and mechanical properties. Another strategy to improve mechanical properties can be related to depositing an inner coating using acid-catalyzed sol and an external coating from a base-catalyzed sol [34,35]. In the field of acid-catalyzed sols, TEOS as a SiO_2 precursor has been successfully combined with organic molecules such as poly(diallyldimethylammonium chloride) [13], polyvinyl acetate [14] or assisted by the presence of surfactants as structuring direct agents (SDA), such as cetyltrimethylammonium chloride [15,16], cetyltrimethylammonium bromide (CTAB)/polypropylene glycol (PPG) mixture [28]. The mixture of TEOS and MTES as SiO_2 precursors has been studied assisted by polyethylene glycol (10) octadecyl ether (Brij76) [18], t-octylphenoxypolyethoxyethanol (Triton X-100) [19–22] and Triton X-100/polyethylene glycol mixture [24]. Other research works reported materials composed by several layers either as composite or layer stack with enhanced features such as self-cleaning or photocatalysis. For example, Li et al. [28] have modelled and synthesized bi-layer SiO_2 stack based on sol-gel with several molar ratio of CTAB/ PPG mixture as surfactant to obtain coating stacks combining materials with refractive index of 1.15 and 1.32 (at 550 nm) and thickness of 154 nm and 134 nm with the aim of obtaining excellent transmittance values at 532 nm and 1064 nm. Poly(ethylene oxide)-b-poly(propylene oxide)-*b*-poly(ethylene oxide) tri-block copolymer (Pluronic F127) is also a very commonly used SDA, and it has been reported for deposition of porous SiO_2 as part of multilayer stack with TiO_2 coatings [25–27]. In those studies, TiO_2 is intended to provide self-cleaning and photocatalytic properties, even though its incorporation has a detrimental effect in optical properties. To avoid this drawback Faustini et al. [26] have prepared porous SiO_2 with refractive index 1.23 (at 700 nm) and an external very thin coating of TiO_2.

Despite tailored refractive index coating deposition is a well-known subject in the state of the art, no much work has been found that experimentally obtains AR layer stack showing the theoretically optimized transmittance values in the range of multijunction cells operation.

This work is focused on the design and deposition of AR multi-layer stack for CPV application providing high transmittance values, spectrally tailored to the spectral response of multijunction solar cell. Since CPV technology is based on low cost optical elements, AR coating feasibility depends on the ratio between the coating processing cost and the enhanced efficiency of the photovoltaic system. Therefore, it is important to optimize the chemical process in order to find conditions that lead to very stable sols with extended pot life that permits to deposit repetitive coatings over time. A suitable AR coating stack should also ensure mechanical properties to withstand long-term durability with minimum transmission losses. An easy and efficient approach is presented herein, based on TEOS, acid catalysis and the use of four types of surfactants as SDA to generate robust processes and products useful to constitute an optimized AR multi-layer stack for glass substrates. AR bi-layer stack was successfully developed by deposition of sols with optimized organic/inorganic phases in order to obtain each single coating with the refractive index, porosity and thickness values that lead to obtain broadband AR performance required in CPV applications.

2. Experimental procedure

2.1. Materials

Absolute ethanol (purity 99.9%) was purchased from Scharlau and

precursor tetraethyl orthosilicate (TEOS, purity 98%) from Acros. They were used as received. Catalyst hydrochloric acid (HCl, 37% vol) was purchased from Scharlau and was used to prepare a 0.1 M solution in distilled water. Surfactants polyethylene glycol (20) hexadecyl ether di-block copolymer (the commercial name is Brij58, denoted here as SDA1), cationic cetyltrimethylammonium bromide (CTAB, denoted here as SDA2), poly(ethylene oxide)-*b*-poly(propylene oxide)-b-poly (ethylene oxide) tri-block copolymer (the commercial name is Pluronic F127, denoted here as SDA3) and t-octylphenoxypolyethoxyethanol di-block copolymer (the commercial name is Triton X-100, denoted here as SDA4) were purchased from Sigma-Aldrich and used as received.

Optiwhite® low iron soda lime float glass (4 mm thick) from Pilkington was used as substrate.

2.2. Design of AR multi-layer stack

CODE® software [52] was used for the design of an optimal optical configuration of the multi-layer stack. In this tool, optical spectra of thin layered systems are obtained from parameterized physical models fitted to provide the desired optical performance.

Several systems composed by low iron float glass as substrate and AR multi-layer stack on it were studied in order to obtain layer properties that minimizes total reflection of the system. An example of tetra-layer stack is shown in Fig. 2, in which reflection vectors at each interface are defined by Eqs. (1)–(5).

The input optical characteristics of low iron float glass were obtained by experimental transmittance and reflectance spectra measured as explained in Section 2.5. Over that substrate, multi-layer stacks were built. Each layer material of the multi-layer stack was defined by Bruggeman medium effective approximation model (BEMA) [53] as a composite formed by SiO_2 matrix in which voids (vacuum) are embedded (Eq. (10)). These calculations permit to obtain the spectral refractive index, void fraction and thickness of each layer of the stack and to select the multi-layer stack that better fits the minimization of selected function. Eventually, reflectance value between 300 and 2000 nm was the function selected for minimization.

In the reflection equations (Eqs. (1)–(5)) of Fig. 2, medium *0* is air, medium *s* is the substrate, and media *1* to *4* correspond to each layer. R_{xy} is the reflection at each interface between *x* and *y* media; n_n is the real part of the refractive index of each material; and δ_n is the phase angle generated by each layer, defined by Eq. (6).

$$R_{01} = \frac{n_0 - n_1}{n_0 + n_1} \tag{1}$$

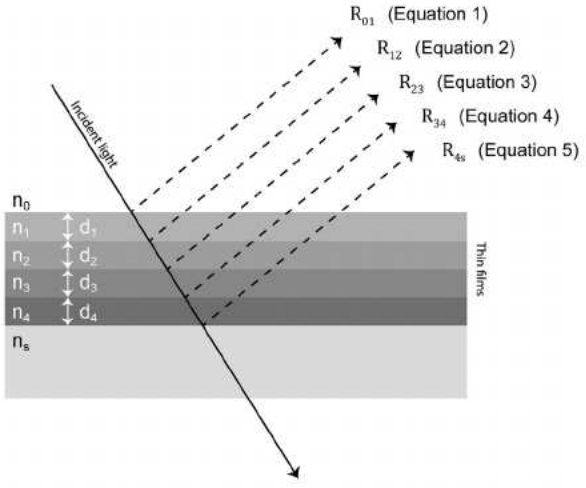

Fig. 2. Physical description of reflection between interfaces in the multi-layer stack.

$$R_{12} = \frac{n_1 - n_2}{n_1 + n_2} \exp^{-2(\delta_1)} \tag{2}$$

$$R_{23} = \frac{n_2 - n_3}{n_2 + n_3} \exp^{-2(\delta_1 + \delta_2)} \tag{3}$$

$$R_{34} = \frac{n_3 - n_4}{n_3 + n_4} \exp^{-2(\delta_1 + \delta_2 + \delta_3)} \tag{4}$$

$$R_{4s} = \frac{n_4 - n_s}{n_4 + n_s} \exp^{-2(\delta_1 + \delta_2 + \delta_3 + \delta_4)} \tag{5}$$

$$\delta_n = \frac{2\pi n_n \cos\theta_n d_n}{\lambda} \tag{6}$$

in which θ_n is reflection angle of each layer, d_n is layer thickness and λ is wavelength.

Considering that outstanding mechanical properties are requested to the external surface of AR multi-layer stack, theoretical calculations were also performed restricting the value of the void fraction of each layer to 50%.

2.3. Preparation of sols

Silica sols were prepared via acid catalysis following a two steps procedure. In a first step, TEOS, ethanol, acidified water (0.1 M HCl) in molar ratio 1:5.6:1.3 and the 4 different SDA mentioned before with concentration from 25 to 150 g/L were mixed and stirred for 90 min at 60 °C. Sol with no SDA was also prepared as baseline. In a second step, a mixture of ethanol and acidified water (0.1 M HCl) in molar ratio 1:0.48 was added drop by drop to the solution and was stirred for 60 min at 40 °C. Ethanol quantity was adjusted in a final stage since depending on final molar ratio between TEOS:ethanol, two different equivalent concentration of SiO_2 were prepared. Sols with ratio 1:8.7 were denoted as high-SiO_2 concentrated (H-sol) and 1:22.5 or 1:24 were denominated low-SiO_2 concentrated (L-sol). Table 1 summarizes the formulations that were prepared. The resultant sols were aged in sealed glass containers for 2 days.

2.4. Preparation of mono-layers

Silica sols were deposited on the low iron float glass 4 mm thick specimens after being cleaned in ethanol under sonication for 15 min and then air dried. Coating deposition was performed onto both sides of the low iron float glass by dip coating at controlled withdrawal rate of 5 cm/min. After coating deposition, sintering step was performed in conventional furnace at 450 °C in air atmosphere for 1 h.

2.5. Characterization

Ellipsometric parameters ψ and Δ, which are functions of the complex refractive index ($\tilde{n} = n + ik$), were recorded by variable angle spectroscopic ellipsometer (M-2000UTM, J.A. Co., Woollam). Spectra

Table 1
Reactants molar ratio, SiO_2 concentration (high, H; low, L), type and concentration of surfactants in the studied sol formulations.

Molar ratio TEOS:H_2O:EtOH	SiO_2 concentration	Surfactant	Surfactant concentration (g/L)
1:4:8.7	H	–	0
1:4:8.7	H	SDA1	25, 50, 100, 150
1:4:22.5	L	SDA1	50, 75
1:4:8.7	H	SDA2	25, 50, 100, 150
1:4:22.5	L	SDA2	50, 75
1:4:8.7	H	SDA3	25, 50, 100, 150
1:4:22.5	L	SDA3	50, 75
1:4:8.7	H	SDA4	25, 50, 100, 150
1:4:24	L	SDA4	50, 75

were recorded from 250 to 1000 nm at three angles of incidence (60°, 65°, 70°). The spectra were fitted using both the Cauchy dispersion model [54] and Bruggeman medium effective approximation model [53]. The fitting allowed the calculation of relevant parameters such as refractive index, *n*, extinction coefficient, *k*, coating thickness, *d*, and porosity. The apparent porosity was calculated with respect to pure dense silica and a polarization factor of 0.33 was considered. The data analysis was performed with WVase32 software.

Cauchy model [54] sets up a simple empirical dispersion law to obtain complex refractive index ($\tilde{n} = n + ik$) parameters (Eqs. (7) and (8)) applied for materials with no optical absorption in the visible spectral range. It does not take into account the nature of the material. However, effective medium theory [55] establishes the connection between the microstructure of a heterogeneous thin film and its macroscopic dielectric response. In our case, the material is composed by a SiO_2 matrix with embedded voids. Bruggeman [53] proposed the approximation of equalizing the effective medium to surrounding environment (Eq. (9)).

$$n(\lambda) = A + \frac{B}{\lambda^2} + \frac{C}{\lambda^4} \tag{7}$$

$$\kappa(\lambda) = D + \frac{E}{\lambda^2} + \frac{F}{\lambda^4} \tag{8}$$

In which *A*, *B*, *C*, *D*, *E*, F are the Cauchy model parameters and λ is the wavelength.

$$c_1 \frac{\tilde{n}_1^2 - \tilde{n}_e^2}{\tilde{n}_1^2 + 2\tilde{n}_e^2} + c_2 \frac{\tilde{n}_2^2 - \tilde{n}_e^2}{\tilde{n}_2^2 + 2\tilde{n}_e^2} = 0 \tag{9}$$

In which $\tilde{n}_1$, $\tilde{n}_2$ and $\tilde{n}_e$ are the complex refractive index of material 1, material 2 and environment respectively, c_1 and c_2 the volume fraction of each material of the coating.

Water adsorption-desorption was studied by environmental ellipsometric porosimetry (EEP) [56,57]. Measurements were performed with the above described equipment (M-2000UTM, J.A. Co., Woollam), within a cell with controlled relative humidity (RH). In this case, the spectra were taken at a fixed incident angle of 70°, at different RH values. Using the Cauchy fitting model, *n* values were obtained as a function of RH. The absorption-desorption isotherms were calculated using Bruggeman medium effective approximation fitting using the optical characteristics of the dense part of the porous media. Pore size distribution were determined using the modified Kelvin's equation, which takes into account Tolman correction and pore anisotropy proposed by Boissière et al. [56].

Transmittance and reflectance spectra of investigated AR coating stacks were measured with a Jasco V-670 UV–Vis–NIR spectrophotometer equipped with a 150 mm integrating sphere. Spectra were taken in the 300–2000 nm wavelength range. Integrated transmittance, τ, was calculated by weighting transmittance values with AM1.5 solar spectral irradiance [58] according to Eq. (10).

$$\tau = \frac{\int_{\lambda_1}^{\lambda_2} T_\lambda \cdot S_\lambda d\lambda}{\int_{\lambda_1}^{\lambda_2} S_\lambda d\lambda} \tag{10}$$

where T_λ is the transmittance spectrum of the covered glass, S_λ is the AM1.5 solar spectrum [58] and λ_1 and λ_2 define the wavelength range where τ is calculated. Integrated reflectance, ρ, was calculated in a similar way using reflectance spectrum instead of transmittance. Gain value, G, was calculated as the percentage of the increment of τ value of coated glass over bare glass $[(\tau_{coat}-\tau_{glass})/\tau_{glass}\cdot 100]$. Minimization value, M, was calculated as the percentage of decrement of ρ value of coated glass below bare glass $[(\rho_{glass}-\rho_{coat})/\rho_{glass}\cdot 100]$.

Kinematic viscosity of sols was measured at 22 °C by means of Ubbelohde viscometer through which the liquid flows through a capillary tube due to its gravity. Different types of capillary tube were used depending on viscosity values, thus type 0B was used for sols with kinematic viscosity between 1 and 5 cSt and type 1 C was used for sols with kinematic viscosity between 6 and 30 cSt. Dynamic viscosity (μ) was obtained by multiplying kinematic viscosity and density that was previously determined with pycnometer/specific gravity bottle. The stability of final liquid sols, which is related to pot-life, was characterized by viscosity measurements along six months after preparation. Viscosity increase, was calculated as the percentage of the increment of viscosity after certain aging time over initial value presented for each sol $[(\mu_{aging}-\mu_{initial})/\mu_{initial}\cdot 100]$.

The surface of investigated coatings was analyzed using atomic force microscopy (AFM). AFM phase and height images were collected by operating in tapping mode with a scanning probe microscope Multimode 8 from Bruker with Nanoscope V controller. The AFM was equipped with an integrated silicon tip/cantilever having a resonance frequency of ~300 kHz and spring constant 42 N m^{-1}. Scan rates ranged from 0.7 to 1.2 Hz s^{-1}. In order to get repeatable results, different regions of the investigated coatings were scanned to choose representative AFM images. Considering that both height and phase AFM images were very similar only AFM phase images are shown here.

3. Results and discussion

3.1. Theoretical optical performance of simulated AR coating stacks

Multi-layer stacks were designed using CODE software [52] by minimizing the total reflection in the 300–2000 nm range. Table 2 shows theoretical optical characteristics of each layer integrated in mono-, bi-, tri- and tetra-layer stacks on both sides of a 4 mm thick low iron float glass (experimental $\tau_{300-2000}$ = 90.1% and $\rho_{300-2000}$ = 8.5%) as well as its integrated transmittance and reflectance values for both free and restricted void fraction.

Higher transmittance value in the whole operation range was achieved for tri-layer stack with growing void fraction layers of 11%, 45% and 77%. Nevertheless, considering that such a high porosity

Table 2
Theoretical calculation of refractive index (n) at 700 nm, void fraction and thickness (d) of layers in mono-, bi-, tri- and tetra-layer stacks and the integrated transmittance (τ) and reflectance (ρ) values between 300 and 2000 nm on 4 mm thick low iron float glass.

Free void fraction							Restricted void fraction						
	Layer	n	Void fraction (%)	d (nm)	τ (%)	ρ (%)		Layer	n	Void fraction (%)	d (nm)	τ (%)	ρ (%)
Mono-layer	1	1.23	48	117	96.4	2.3	Mono-layer	1	1.23	48	117	96.4	2.3
Bi-layer	1	1.14	67	127	97.8	0.8	Bi-layer	1	1.22	50	119	97.4	1.4
	2	1.34	24	107				2	1.41	10	106		
Tri-layer	1	1.10	77	129	98.3	0.3	Tri-layer	1	1.22	50	115	97.4	1.2
	2	1.24	45	114				2	1.35	22	100		
	3	1.40	11	100				3	1.45	0	80		
Tetra-layer	1	1.10	77	113	98.3	0.3	Tetra-layer	1	1.22	50	114	97.4	1.3
	2	1.03	93	10				2	1.35	21	110		
	3	1.24	45	117				3	1.43	5.5	6		
	4	1.40	11	100				4	1.44	2.5	96		

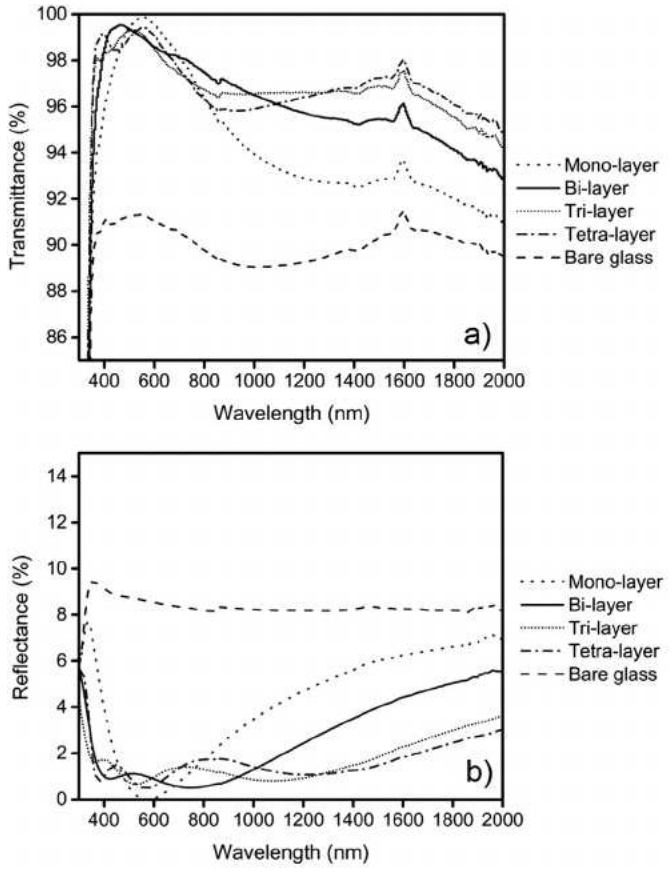

Fig. 3. Transmittance (a) and reflectance (b) spectra of different optimized multi-layer stacks (porosity value restricted to 50%).

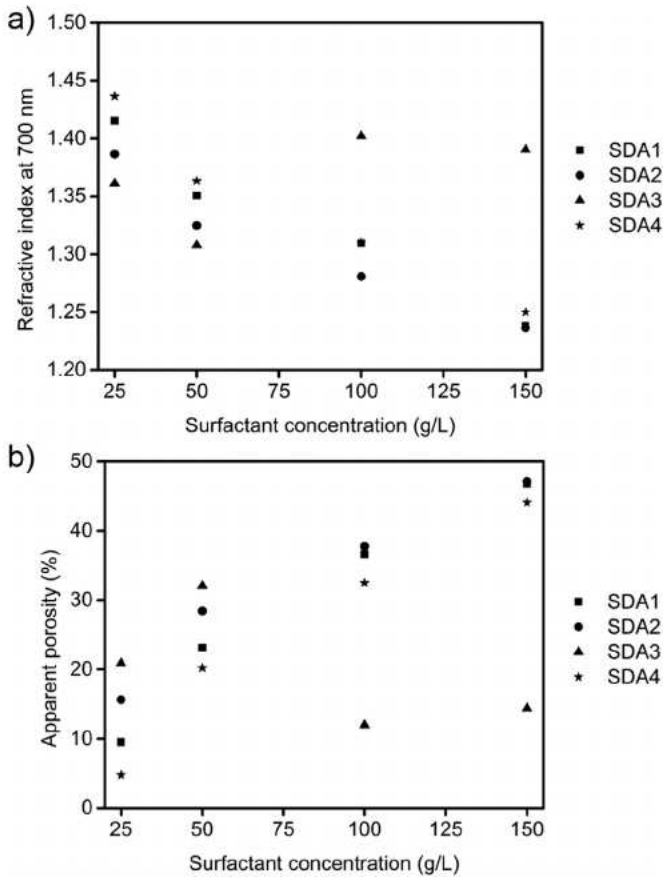

Fig. 4. Effect of surfactant concentration on refractive index (a) and porosity (b) of coatings obtained from H-sols. (n ± 0.001; Apparent porosity ± 0.2%).

would result in very fragile layers with poor mechanical properties, the void fraction of external layer was restricted to 50%. In this scenario, integrated transmittance value was similar for bi- and tri-layer stacks. However, as shown in Fig. 3, spectral differences were found in transmittance and reflectance curves. In the 400–980 nm range, the integrated transmittance values of bi-layer stack were higher than the corresponding values of tri-layer stack while in the 980–2000 nm range, the integrated transmittance values of tri-layer stack were higher than those of the bi-layer stack.

In most current multijunction solar cell configurations, top and middle subcells operate in the range between 350 and 900 nm, and bottom cell operates between 900 and 1800 nm. Usually the top and middle subcells generate similar current density while the bottom cell over generates current [5]. Therefore, the latter is not the one which limits the current of the total series connected cells, and decisive parameters concern the top and middle subcells range. Taking the above into consideration, bi-layer stack composed by an inner layer with 1.41 refractive index at 700 nm and 106 nm thick and outer layer with 1.22 refractive index at 700 nm and 119 nm thick, was selected as target for experimental development as discussed below.

3.2. Effect of surfactant type and concentration on void fraction and refractive index

It is known that EISA method is a complex approach due to the chemical and physical phenomena involved [47]. Depending on the ratio between inorganic and organic parts, the solvent, and the quantity of water as well as the processing conditions, the structures of prepared coating material can be controlled. For this reason, four types of organic/inorganic systems were scanned in order to obtain coatings with 50% of void fraction. Single coatings grown on glass with H-sols using different weight concentration for four different surfactants as organic templates were studied. Refractive index and apparent porosity of these coatings as a function of surfactant concentration are represented in Fig. 4a and in Fig. 4b, respectively. It is clearly observed that for H-sols with SDA1, SDA4 and SDA3, the increase of organic phase resulted in coatings with lower refractive index and consequently higher porosity, arriving to the targets as predicted by theoretical calculation.

Coatings grown with the SDA2-sols reached a maximum value of porosity at surfactant concentration of 50 g/L while sols with higher concentration did not form higher porosity in coatings.

It is also noticeable that for lower surfactant concentrations, 25 and 50 g/L, the highest porosity was detected for SDA2-sols, followed by SDA4-sols, SDA1-sols and SDA3-sols, what is in good agreement with the increase of molecular weight of the organic surfactants. Other remarkable result was that for surfactant concentration equal to 150 g/L, SDA2 excluded, the differences between organic surfactants were reduced and porosity merged into a similar value close to 50%, what agreed with theoretical prediction.

3.3. Effect of surfactant type and concentration on coating thickness

Several forces contribute to coating formation and derived thickness during withdrawal of substrate from sol, such as dragging force, gravity, forces related to liquid surface tension and to the interaction between solid specimen and liquid [59]. Most of these factors are inherent of the system and other such as dragging force can be controlled since it is proportional to viscosity of sol and withdrawal rate. Therefore, viscosity of H-sols was studied as a function of surfactant concentration and presented in Fig. 5a. Viscosity of sol without SDA was 2 mPa·s. This sol was useful for growing dense coating onto glass. As explained before, different surfactant concentration was scanned in

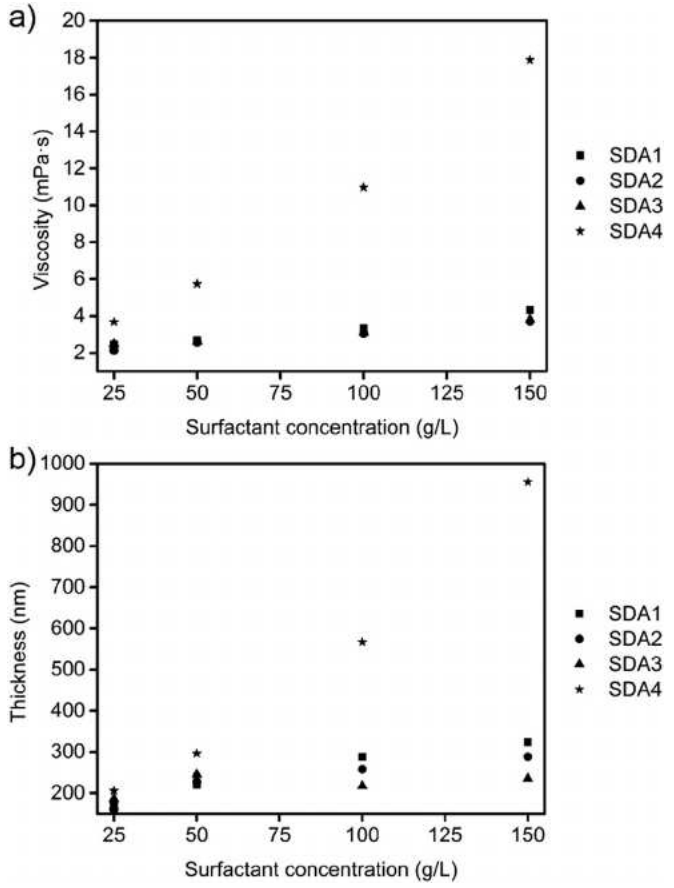

Fig. 5. Effect of surfactant concentration on viscosity of H-sols (a) and thickness of derived coatings (b). (Viscosity ± 0.05 mPa s; Thickness ± 1 nm).

order to achieve porosity of 50%. In this experimental scanning, difference for each surfactant was observed when viscosity value increased with increase of surfactant concentration. Viscosity of H-sols based on SDA1, SDA2 and SDA4 varied from 2.3 ± 0.2 mPa s for 25 g/L of surfactant concentration to 4.0 ± 0.3 mPa·s for 150 g/L of surfactant concentration while viscosity of H-sols with SDA3 varied from 3.7 to 17.9 mPa s for the same surfactant concentration as before. The Landau-Levich equation [60] which describes the thickness by the equilibrium between the adhesion of the fluid on the substrate and gravity-induced viscous drag, predicts that the thickness is proportional to the viscosity of the fluid at the power of 2/3. Taken this into account, higher viscosity sols will lead to form higher coating thickness.

Such wide range of obtained sol viscosities leaded to a broad spread of thickness values for derived coatings as shown in Fig. 5b. As expected, similarly to trend in the viscosity, the coating thickness increased in the function of surfactant concentration. Coatings without SDA presented thickness of 121.0 nm. Thickness of coatings based on SDA1 and SDA4-sols expanded from around 170 nm for 25 g/L surfactant concentration to around 300 nm for 150 g/L surfactant concentration while thickness of coatings based on SDA3 sols expanded from around 200 nm to almost 1000 nm, for the same surfactant concentration as before. The exception was coatings based on SDA2 surfactant, since the coatings formed with these sols at highest concentration did not present the expected increase of thickness. This result is in good agreement with low porosity values obtained for these coatings.

Anyhow, optimum thickness value should be accompanied with optimum porosity value to obtain optimum value of transmittance. Therefore, although H-sols permitted to prepare layers with porosity around 50%, the obtained thickness values did not fit with the requirements to be candidate for AR multi-layer stacks.

Evolution of viscosity of H-sols with and without SDA was monitored up to six months of aging. The viscosity increase of H-sol without SDA was around 18% after six months of aging. Only sols prepared with SDA1 and SDA4 were stable after that time in the whole surfactant concentration range tested, understanding as stable sols those which maintained their transparent, fluid, and one-phase status. The viscosity increase for sols with SDA1 after six months was in decrescent order, 15% for sol with 25 g/L, 9% for sol with 50 g/L, 5% for sol with 100% while no increase was detected for sol with 150 g/L. The viscosity of sol with 25 g/L SDA4 doubled its value after six months of aging. However, sols with 50, 100 and 150 g/L of SDA4 maintained their initial value after six months of monitoring. In these cases, the presence of organic phases, contributed to improve the viscosity stability of sols as long as their concentration increased. Among sols prepared with SDA2, only those prepared at 25, 50 and 100 g/L were stable after six months, and their viscosity increased in 2%, 10% and 4% respectively while that prepared with 150 g/L was not stable after one week. The viscosity increase after one month of ageing of sols prepared with SDA3 was around 7–8% for 25, 100 and 150 g/L concentrations while no increase was detected for sol prepared with 50 g/L. After one month, they became a two-phase separation and further measurements did not occur.

3.4. Textural properties (EEP & AFM)

Investigated porous coatings were analyzed by environmental ellipsometric porosimetry (EEP). This is a non-destructive technique that obtains the amount of adsorptive inside of pores from the change of optical characteristics of the coatings (thickness and refractive index) measured at several water partial pressures. Adsorption-desorption curves of coatings from H-sols based on different surfactants with 50 g/L surfactant concentration and their pore size distribution are showed in Fig. 6. The surfactant concentration of sols was selected due to this is a common concentration at which derived coatings presented most similar porosity values. The typical behavior of mesoporous materials associated with isotherms type IV was observed for all coatings. The hysteresis loops appear due to the difference of radius of curvature of condensed liquid meniscus during the adsorption and desorption processes in the mesopores [57]. Its shape can be further correlated to the texture (e.g., pore size distribution, pore geometry, and connectivity) of a mesoporous material [61] according to an empirical classification in four types of curves given by IUPAC. Hysteresis loops of all coatings were identified as type H1, which exhibits parallel branches and is associated with porous materials consisting of well-defined cylindrical-like pore channels or agglomerates of approximately uniform spheres. For coatings deposited from sols with the same surfactant concentration, total volume of pores was 20% for SDA3, 30% for SDA1 and about 35% for both SDA2 and SDA4.

Pore size distribution was determined using modified Kelvin's equation [56] and, as mentioned above, results are included in Fig. 6. SDA4, SDA2 and SDA1 coatings showed a narrow pore size distribution with maximum at 6, 7 and 4.5 nm, respectively, while SDA3 coating exhibited a bi-modal distribution with pores around 6.5 and 9 nm.

Fig. 7 shows the AFM phase images of coatings obtained from H-sols with 50 g/L of different surfactants as well as H-sol with no surfactant content. It can be observed that the surface of investigated coatings was crack free and homogenous. The resulting topography of the porous coatings was composed of small grains that apparently without any particular order. SDA1 and SDA4 coatings presented grains of around 12 ± 2 nm, however in the case of SDA4 coating some aggregated can be distinguished on the investigated surface. SDA2 and SDA3 coatings were formed by smaller grains of 6 ± 2 nm and 5 ± 1 nm, respectively. Image root mean square (RMS) roughness (R_q) of porous coatings was in rising order, 0.7 nm for SDA1 coating, 1 nm for SDA3 coating, 1.2 nm for SDA4 coating and 1.7 nm for SDA2 coating. Topography of dense coating resulted in a smooth surface since it did not

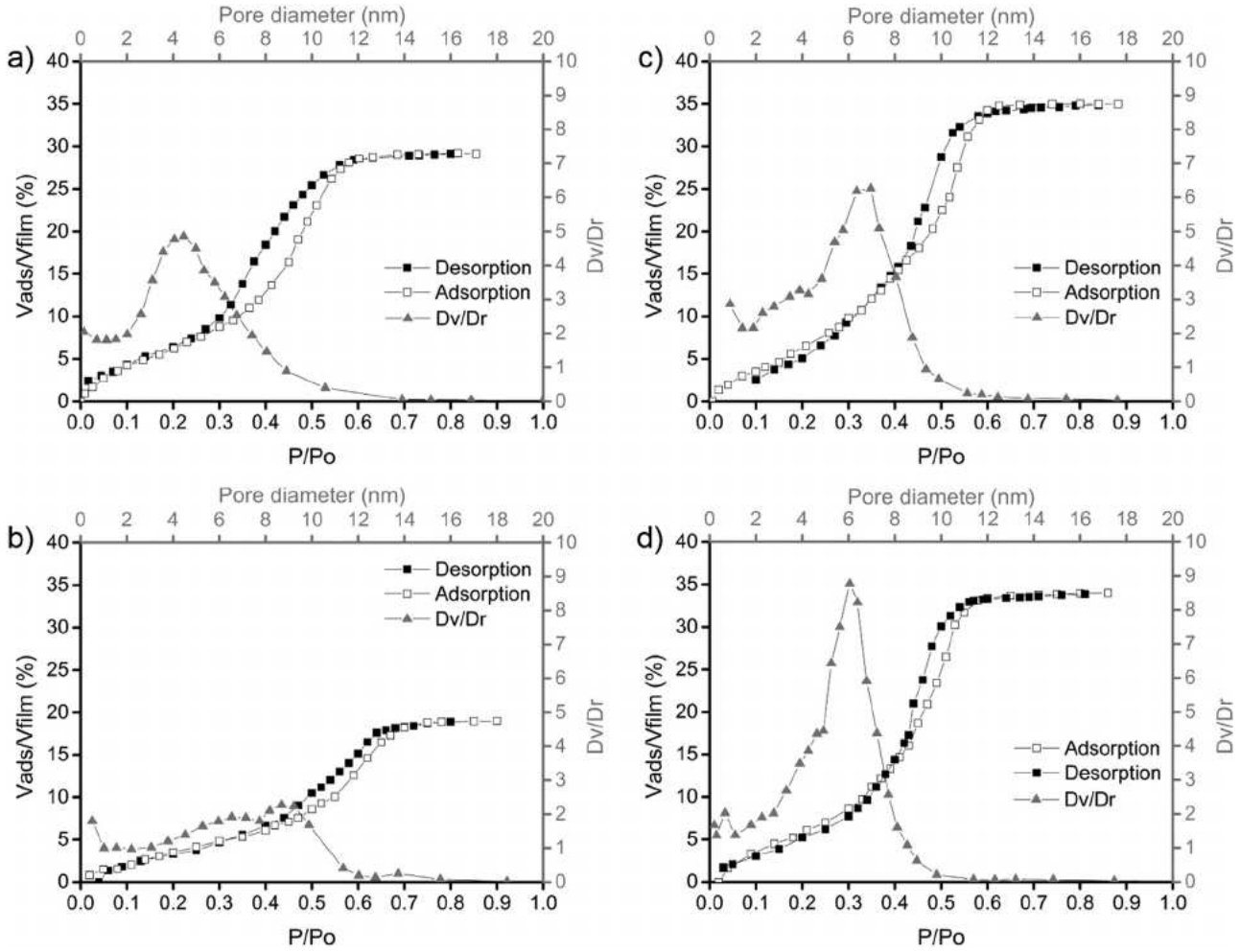

Fig. 6. Adsorption/desorption isotherms and pore size distribution of coatings obtained from H-sols with 50 g/L of SDA1 (a), SDA2 (b), SDA3 (c) and SDA4 (d).

present void fraction, although R_q was 2.4 nm, higher than porous coatings roughness. Consequently, there was not a proportional relation between observed grain size and surface roughness.

3.5. Final optimization of formulation

As explained before, as long as surfactant concentration increased in the sol formulation both porosity and thickness of the deposited coating followed the same tendency. Since the coating structural features such as refractive index and porosity do not vary with the thickness [62], it could have been appropriate to modify withdrawal rate in order to obtain thinner coatings with such obtained porosity. However, lower withdrawal rate did not provide thinner coatings, what permitted to conclude that operating conditions were near to critical withdrawal speed between draining and capillarity regime, in which at low speeds, the thickness increases when speed decreases [62]. Taken this into account, new formulations with lower concentration of equivalent SiO_2, L-sols, were prepared in order to be capable to obtain the proper conditions. Theoretical concentration of SiO_2 in these new sols was about 35 g/L, with surfactant concentration of 50 and 75 g/L however maintaining molar ratio of TEOS:surfactant as in cases of 100 and 150 g/L of H-sols. Optical properties of these L-sol coatings were calculated by ellipsometry and are shown in Table 3. Analysis of thickness and refractive index showed that when the surfactant concentration increased from 50 to 75 g/L the increase of thickness was observed simultaneously, refractive index showed lower values and therefore porosity got higher values. Furthermore, the increase of thickness was more pronounced when porosity increase was higher. As observed with H-sols, SDA3 concentration caused the biggest effect on thickness and porosity. In this case, coating porosity raised 25% when increasing concentration from 50 to 75 g/L in the same way as thickness. In the case of SDA4-sols, the thickness and porosity differences were almost negligible.

Coatings prepared from SDA1- and SDA4-sols presented acceptable thickness, while SDA2-sols formed too thin coatings and SDA3-sols yet generated too high thickness. The coating that best matched thickness and refractive index values corresponded to formulation with 75 g/L of SDA1. Viscosity did not increase in L-sols prepared with SDA1, SDA2 and SDA4 after six months with exception of SDA2 and SDA4 both at 75 g/L that became unstable. Viscosity of sols with SDA3 was constant after one month of aging.

Fig. 8 shows the AFM phase images of coatings obtained from L-sols with 50 g/L of different surfactants. Coatings deposited from SDA1-, SDA3- and SDA4-sols showed crack free surface and homogeneously distributed voids. Coating derived from SDA3-sol showed mesostructured porosity since grains are ordered showing a fingerprint structure. SDA1 and SDA4 coatings did not show any mesostructure. Coating obtained with SDA2-sol presented some inhomogeneities, like different grain size and aggregates. Rq of coatings was 0.9 nm for SDA1 coating, 1.2 nm for SDA4 coating and the highest values as 3 nm for SDA3 mesostructured coating, and 4.6 nm for SDA2 inhomogeneous coating.

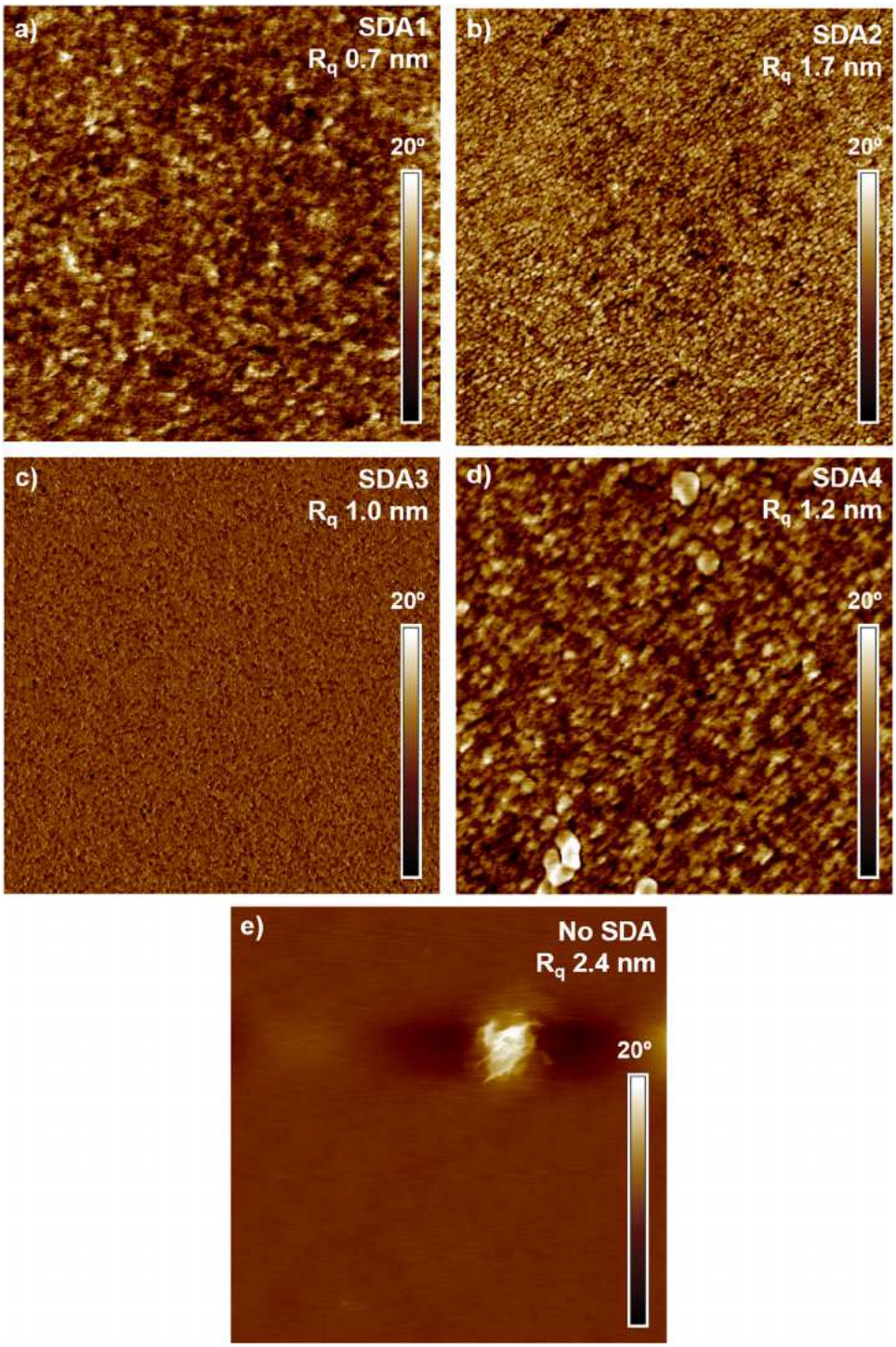

Fig. 7. AFM phase images (1 μm × 1 μm) of coatings obtained from H-sols with 50 g/L of SDA1 (a), SDA2 (b), SDA3 (c), SDA4 (d) and without SDA (e).

3.6. Antireflective properties

Transmittance and reflectance spectra of bare and double side coated low iron glass with L-sols prepared with surfactant concentration of 50 and 75 g/L are depicted in Fig. 9. It was clearly observed that both spectra for each coating were consistent, showing corresponding maxima and minima at equal wavelengths. Analysis of the spectra showed that maximum values in transmittance spectra were settled in the range 550–600 nm for coatings deposited with SDA1-, SDA2- and SDA4-sols. Within this range, when increasing surfactant concentration from 50 to 75 g/L maximum of SDA1- and SDA2-sols derived coatings, was little shifted from lower to higher wavelength while maximum in coatings with SDA4 did not move. These results are related to obtained variation in the coating thickness. In the case of SDA3-sols derived coatings which presented the highest thickness values, the maximums were around 700 and 1370 nm for 50 and 75 g/L of surfactant, respectively.

Nonetheless, higher transmittance / lower reflectance integrated values along the whole spectrum were clearly obtained for coatings deposited from SDA1- and SDA4-sols. Integrated values calculated in the 300–2000 nm spectral range are compiled in Table 4. Attending to these, coatings deposited with both SDA1-sols showed the best results.

Table 3
Refractive index (n) at 700 nm, porosity and thickness (d) of coatings obtained from L-sols by spectral ellipsometry.

	n	Porosity (%)	d (nm)
L-SDA1-50 g/L	1.28	37.3	120
L-SDA1-75 g/L	1.25	45.3	126
L-SDA2-50 g/L	1.41	10.9	88
L-SDA2-75 g/L	1.34	23.7	98
L-SDA3-50 g/L	1.39	15.1	142
L-SDA3-75 g/L	1.27	40.4	258
L-SDA4-50 g/L	1.29	36.3	117
L-SDA4-75 g/L	1.28	38.8	112

Particularly, sol with 75 g/L of SDA1 allowed preparing the porous coating with proper thickness and refractive index which permitted to obtain the highest reflection reduction among the mono-layers studied (as low as 2.7%) being 68% (M) lower than bare low iron float glass. Consequently, gain in transmittance was 6% (G) over bare low iron float glass.

Considering this outcome, the bi-layer stack designed with CODE software was intended to be assembled onto float glass. Another crucial factor was considered for the design of stack, concerning glass composition and alkali diffusion. Most float glass is composed by silica and a mixture of alkali and metal oxides [2]. In some applications like solar industry, low iron content is willfully used in order to improve solar transmittance despite its higher cost production. However, content of sodium, calcium, potassium, magnesium is always kept in glass body and can diffuse out of the glass when it is used for an extended period of time, leading to decrement of optical properties [63]. One way to avoid this degradation is to deposit a dense coating for preventing diffusion of elements from glass body. Consequently, the intention was to use inner layer of the stack as diffusion-preventing-layer. Therefore, the inner layer was preferred to have dense structure, using H-sol without SDA. This coating was 121.0 nm thick with 1.41 refractive index at 700 nm. The external layer was deposited from L-sol with 75 g/L of SDA1. Fig. 10 depicts spectral reflectance of single and bi-layer stack on both sides of low iron float glass, so as to bare glass.

Both mono- and bi-layer stacks provided a transmittance increase in the whole spectral range compared to the bare substrate however the combination of the two layers permitted to obtain lower reflectance in the whole spectrum therefore improved broadband AR properties. Minimum reflectance value was obtained at 685–690 nm for single coating and at 550–560 nm for bi-layer, and integrated value between 300 and 2000 nm dropped up to 1.7% which means a reflection minimization of 80% over the bare low iron float glass versus the minimization of 68% that was achieved with single coating. If stated in transmittance mode, integrated value between 300 and 2000 nm raised up to 96.6%. what means a gain of 7.2% for the bi-layer over the bare low iron float glass versus the 6.0% that was achieved with single coating.

Li et al. [35] built an equivalent stack composed by inner layer from acid-catalyzed sols and outer layer from base-catalyzed coating, and studied transmittance spectra only in the range 400–1000 nm. Moreover, Li et al. [28] built a bi-layer stack composed by two porous layers and studied transmittance spectra only in the range 400–1100 nm focusing in the higher transmittance at 532 and 1064 nm. We propose a

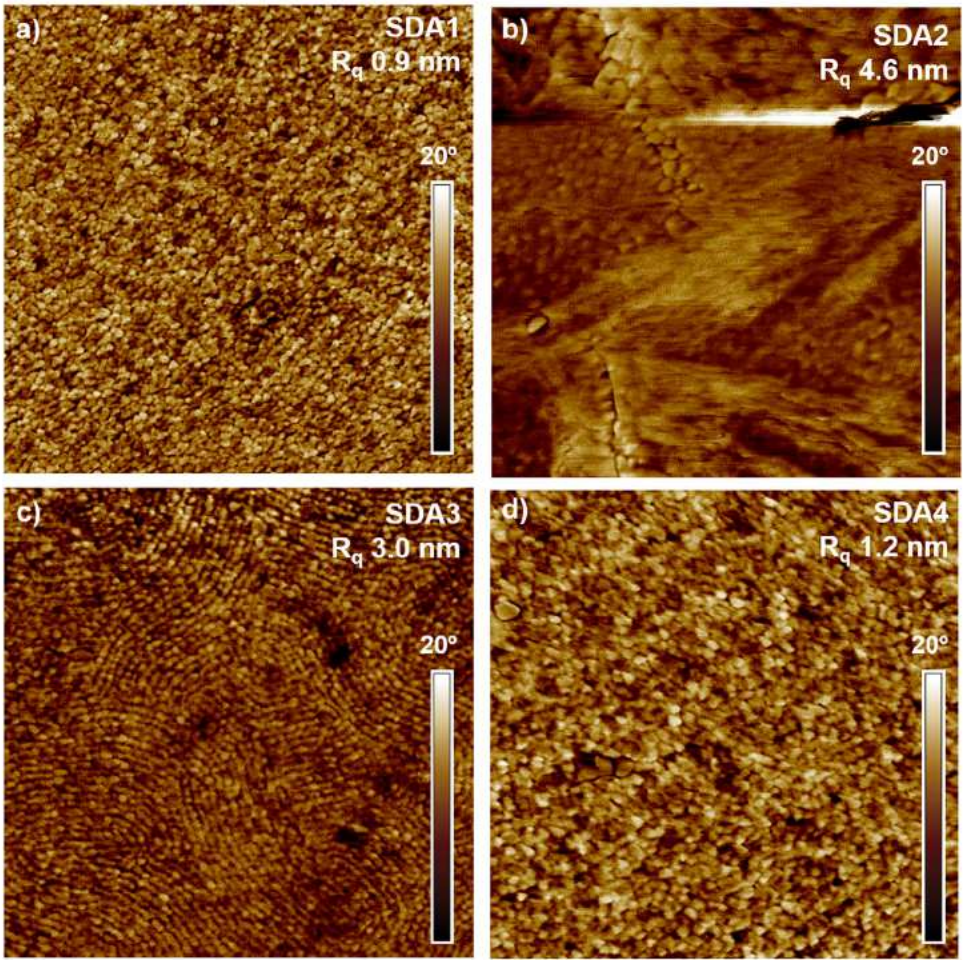

Fig. 8. AFM phase images (1 μm × 1 μm) of coatings obtained from L-sols with 50 g/L of SDA1 (a), SDA2 (b), SDA3(c) and SDA4 (d).

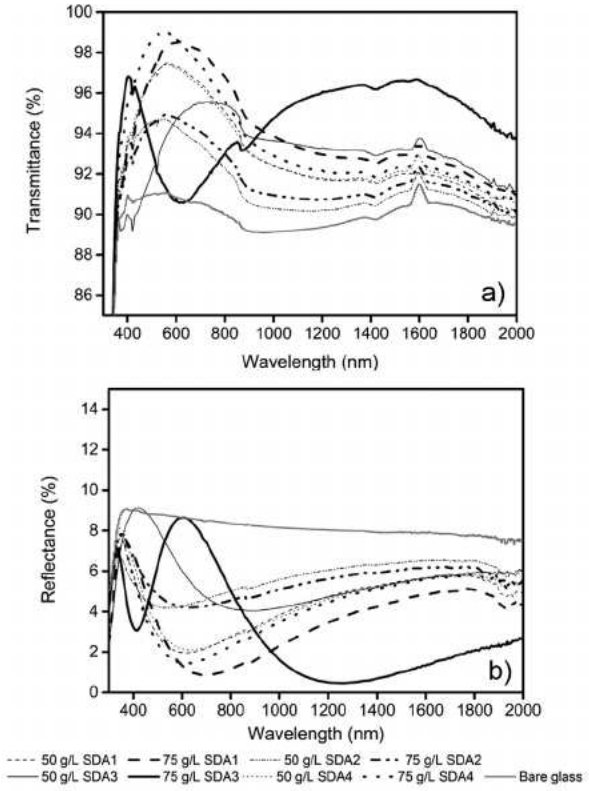

Fig. 9. Transmittance (a) and reflectance (b) spectra of low iron float glass coated on both sides with L-sols.

Table 4
Integrated transmittance (τ) and reflectance (ρ) values between 300 and 2000 nm of coatings obtained from L-sols on both sides of low iron float glass 4 mm thick; gain (G) and minimization (M) over bare glass.

	τ (%)	G (%)	ρ (%)	M (%)
Bare glass	90.1		8.4	
L-SDA1-50 g/L	94.5	4.9	3.4	− 59.1
L-SDA1-75 g/L	95.6	6.0	2.7	− 68.1
L-SDA2-50 g/L	92.4	2.5	5.1	− 39.9
L-SDA2-75 g/L	92.7	2.9	5.0	− 40.5
L-SDA3-50 g/L	93.5	3.7	5.7	− 32.1
L-SDA3-75 g/L	93.3	3.6	4.7	− 44.0
L-SDA4-50 g/L	94.5	4.9	3.6	− 57.8
L-SDA4-75 g/L	95.5	6.0	3.1	− 63.4
Bi-layer	96.6	7.2	1.7	− 79.9

robust process based on acid-catalyzed sols that permits to build a broadband AR multi-layer stack whose material synthesis route and architecture has been specially thought for potentially withstand exposure to the environmental conditions where CPV modules operate [64].

4. Conclusions

Broadband AR multi-layer stack for application on the cover glass of a concentration photovoltaic system was designed and developed [65]. Sol-gel via acid catalysis and evaporation-induced self-assembly (EISA) methods led to mesostructured porous coatings with a high control of the void fraction. Four types of surfactant were used to correlate the theoretical prediction with experimental results. Inner layer was deposited from H-sol, with dense structure, 121.0 nm thick and 1.41 refractive index at 700 nm while L-sol with 75 g/L of SDA1 permitted to obtain the external layer 126.2 nm thick and 1.25 refractive index at 700 nm which are values close to the targets calculated by CODE

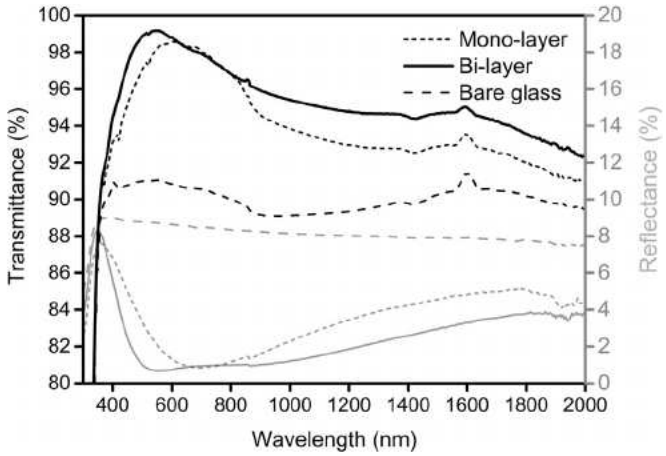

Fig. 10. Transmittance and reflectance spectra of low iron float glass coated on both sides with mono and bi-layer stacks.

software as the optimal optical configuration of the stack.

Eventually graded-refractive-index multilayer system was optimized providing an AR coating stack with minimum reflection loss, being 1.7% for bi-layer deposited on both side of low iron float glass 4 mm thick. The composition and mesostructure was designed to potentially provide high mechanical stability in comparison to other sol-gel synthesis routes followed for preparation of porous coatings (i.e. base-catalyzed sol-gel). This antireflective stack attempts to be an encouraging candidate to fulfil the requirements of photovoltaics standards (e.g. IEC 62108 [66]) regarding durability.

Acknowledgements

This work was supported by the Basque Government for EMAITEK 2017 program as well as the ELKARTEK projects FRONTIERS-2 (Contract no. KK2016-00093) and FRONTIERS-3 (Contract no. KK2017-00096)

This work has received funding from the European Union's Horizon 2020 Research and Innovation Programme within the project CPVMatch under Grant agreement no. 640873. The authors are solely responsible for the content of this work and it only reflects the author's view.

The authors thank ICV-CSIC, Yolanda Castro and Alicia Durán for ellipsometry and EEP measurements.

References

[1] D. Chen, Anti-reflection (AR) coatings made by sol gel processes: a review, Sol. Energy Mater. Sol. Cells 68 (2001) 313–336, http://dx.doi.org/10.1016/S0927-0248(00)00365-2.
[2] K. Burrows, V. Fthenakis, Glass needs for a growing photovoltaics industry, Sol. Energy Mater. Sol. Cells 132 (2015) 455–459, http://dx.doi.org/10.1016/j.solmat.2014.09.028.
[3] J.P. Dunlop, Photovoltaic Systems, American Technical Publishers, Inc., 2012, 〈https://books.google.es/books/about/Photovoltaic_Systems.html?id=qPxeLwEACAAJ&redir_esc=y〉 (Accessed 11 June 2018).
[4] P. Rodrigo, E.F. Fernández, F. Almonacid, P.J. Pérez-Higueras, Models for the electrical characterization of high concentration photovoltaic cells and modules: a review, Renew. Sustain. Energy Rev. 26 (2013) 752–760, http://dx.doi.org/10.1016/j.rser.2013.06.019.
[5] S. Van Riesen, M. Neubauer, A. Boos, M.M. Rico, C. Gourdel, S. Wanka, R. Krause, P. Guernard, New module design with 4-junction solar cells for high efficiencies, AIP Conf. Proc. 1679 (2015), http://dx.doi.org/10.1063/1.4931553.
[6] M.A. Green, K. Emery, Y. Hishikawa, W. Warta, E.D. Dunlop, Solar cell efficiency tables (version 47), Prog. Photovolt. Res. Appl. 24 (2016) 3–11, http://dx.doi.org/10.1002/pip.2728.
[7] M. Buljan, J. Mendes-Lopes, P. Benítez, J.C. Miñano, Recent trends in concentrated photovoltaics concentrators' architecture, J. Photonics Energy 4 (2014) 040995, http://dx.doi.org/10.1117/1.JPE.4.040995.
[8] Y.H. Kang, S.S. Oh, Y.S. Kim, C.G. Choi, Fabrication of antireflection nanostructures by hybrid nano-patterning lithography, Microelectron. Eng. 87 (2010) 125–128, http://dx.doi.org/10.1016/j.mee.2009.06.006.
[9] C.J. Ting, C.F. Chen, C.P. Chou, Subwavelength structures for broadband

antireflection application, Opt. Commun. 282 (2009) 434–438, http://dx.doi.org/10.1016/j.optcom.2008.10.026.
[10] Y. Li, K. Yang, B. Xia, B. Yang, L. Yan, M. He, H. Yan, B. Jiang, Preparation of mechanically stable triple-layer interference broadband antire fl ective coatings with, RSC Adv. 7 (2017) 14660–14668, http://dx.doi.org/10.1039/C7RA00844A.
[11] M. Manca, A. Cannavale, L. De Marco, A.S. Aricò, R. Cingolani, G. Gigli, Durable superhydrophobic and antireflective surfaces by trimethylsilanized silica nanoparticles-based sol-gel processing, Langmuir 25 (2009) 6357–6362, http://dx.doi.org/10.1021/la804166t.
[12] G. Helsch, A. Mös, J. Deubener, M. Höland, Thermal resistance of nanoporous antireflective coatings on silica glass for solar tower receivers, Sol. Energy Mater. Sol. Cells 94 (2010) 2191–2196, http://dx.doi.org/10.1016/j.solmat.2010.07.011.
[13] J.H. Rouse, B.A. MacNeill, G.S. Ferguson, Sol-gel processing of ordered multilayers to produce composite films of controlled thickness, Chem. Mater. 12 (2000) 2502–2507, http://dx.doi.org/10.1021/cm000291a.
[14] H.K. Raut, A.S. Nair, S.S. Dinachali, V.A. Ganesh, T.M. Walsh, S. Ramakrishna, Porous SiO2 anti-reflective coatings on large-area substrates by electrospinning and their application to solar modules, Sol. Energy Mater. Sol. Cells 111 (2013) 9–15, http://dx.doi.org/10.1016/j.solmat.2012.12.023.
[15] X. Meng, Y. Wang, H. Wang, J. Zhong, R. Chen, Preparation of hydrophobic and abrasion-resistant silica antireflective coatings by using a cationic surfactant to regulate surface morphologies, Sol. Energy 101 (2014) 283–290, http://dx.doi.org/10.1016/j.solener.2013.12.038.
[16] Y. Xu, C. Peng, C. Xin, J. Wu, Preparation of silica antireflective films for solar energy application, Mater. Lett. 94 (2013) 89–91, http://dx.doi.org/10.1016/j.matlet.2012.12.013.
[17] Y. Li, H. Lv, L. Ye, L. Yan, Y. Zhang, B. Xia, H. Yan, B. Jiang, Preparation of porous silica films in a binary template system for double-layer broadband antireflective coatings, RSC Adv. 5 (2015) 20365–20370, http://dx.doi.org/10.1039/C4RA17141A.
[18] T.-J. Ha, H.-H. Park, S.-B. Jung, H. Ryu, B.-G. Yu, Investigation of the effect of calcination temperature on HMDS-treated ordered mesoporous silica film, J. Colloid Interface Sci. 326 (2008) 186–190, http://dx.doi.org/10.1016/j.jcis.2008.07.024.
[19] G.S. Vicente, R. Bayón, A. Morales, Effect of additives on the durability and properties of antireflective films for solar glass covers, J. Sol. Energy Eng. 130 (2008) 011007, http://dx.doi.org/10.1115/1.2804626.
[20] G. San Vicente, R. Bayón, N. Germán, A. Morales, Surface modification of porous antireflective coatings for solar glass covers, Sol. Energy 85 (2011) 676–680, http://dx.doi.org/10.1016/j.solener.2010.06.009.
[21] G. San Vicente, R. Bayón, N. Germán, A. Morales, Long-term durability of sol-gel porous coatings for solar glass covers, Thin Solid Films 517 (2009) 3157–3160, http://dx.doi.org/10.1016/j.tsf.2008.11.079.
[22] H.L. Yang, L. Hao, J.N. Wang, Z.N. Zhang, X.P. Liu, L.J. Jiang, Self-cleaning and antireflective films for all-glass evacuated tube solar collectors, Energy Procedia (2015) 226–232.
[23] B.T. Liu, W. De Yeh, Antireflective surface fabricated from colloidal silica nanoparticles, Colloids Surf. A Physicochem. Eng. Asp. 356 (2010) 145–149, http://dx.doi.org/10.1016/j.colsurfa.2010.01.003.
[24] D.B. Mahadik, R.V. Lakshmi, H.C. Barshilia, High performance single layer nanoporous antireflection coatings on glass by sol-gel process for solar energy applications, Sol. Energy Mater. Sol. Cells 140 (2015) 61–68, http://dx.doi.org/10.1016/j.solmat.2015.03.023.
[25] R. Prado, G. Beobide, A. Marcaide, J. Goikoetxea, A. Aranzabe, Development of multifunctional sol-gel coatings: anti-reflection coatings with enhanced self-cleaning capacity, Sol. Energy Mater. Sol. Cells 94 (2010) 1081–1088, http://dx.doi.org/10.1016/j.solmat.2010.02.031.
[26] M. Faustini, L. Nicole, C. Boissière, P. Innocenzi, C. Sanchez, D. Grosso, Hydrophobic, antireflective, self-cleaning, and antifogging sol-gel coatings: an example of multifunctional nanostructured materials for photovoltaic cells, Chem. Mater. 22 (2010) 4406–4413, http://dx.doi.org/10.1021/cm100937e.
[27] L. Miao, L.F. Su, S. Tanemura, C.A.J. Fisher, L.L. Zhao, Q. Liang, G. Xu, Cost-effective nanoporous SiO2-TiO2 coatings on glass substrates with antireflective and self-cleaning properties, Appl. Energy 112 (2013) 1198–1205, http://dx.doi.org/10.1016/j.apenergy.2013.03.043.
[28] Y. Li, H. Lv, L. Ye, L. Yan, Y. Zhang, B. Xia, H. Yan, B. Jiang, Preparation of porous silica films in a binary template system for double-layer broadband antireflective coatings, RSC Adv. 5 (2015) 20365–20370, http://dx.doi.org/10.1039/C4RA17141A.
[29] D. Li, F. Huang, S. Ding, Sol-gel preparation and characterization of nanoporous ZnO/SiO2 coatings with broadband antireflection properties, Appl. Surf. Sci. 257 (2011) 9110–9119.
[30] H.M. Shang, Y. Wang, S.J. Limmer, T.P. Chou, K. Takahashi, G.Z. Cao, Optically transparent superhydrophobic silica-based films, Thin Solid Films 472 (2005) 37–43, http://dx.doi.org/10.1016/j.tsf.2004.06.087.
[31] S. Cai, Y. Zhang, H. Zhang, H. Yan, H. Lv, B. Jiang, Sol-gel preparation of hydrophobic silica antireflective coatings with low refractive index by base/acid two-step catalysis, ACS Appl. Mater. Interfaces (2014) 8–13, http://dx.doi.org/10.1021/am501972y.
[32] H. Ye, X. Zhang, Y. Zhang, L. Ye, B. Xiao, H. Lv, B. Jiang, Preparation of antireflective coatings with high transmittance and enhanced abrasion-resistance by a base/acid two-step catalyzed sol-gel process, Sol. Energy Mater. Sol. Cells 95 (2011) 2347–2351, http://dx.doi.org/10.1016/j.solmat.2011.04.004.
[33] G. Wu, J. Wang, J. Shen, T. Yang, Q. Zhang, B. Zhou, Z. Deng, B. Fan, D. Zhou, F. Zhang, A new method to control nano-porous structure of sol-gel-derived silica films and their properties, Mater. Res. Bull. 36 (2001) 2127–2139, http://dx.doi.org/10.1016/S0025-5408(01)00691-2.
[34] Y. Zhang, F. Gao, L. Gao, L. Hou, Y. Jia, Study of tri-layer antireflection coatings prepared by sol – gel method, J. Sol-Gel Sci. Technol. 62 (2012) 134–139, http://dx.doi.org/10.1007/s10971-012-2697-7.
[35] X. Li, J. Shen, A scratch-resistant and hydrophobic broadband antireflective coating by sol-gel method, Thin Solid Films 519 (2011) 6236–6240, http://dx.doi.org/10.1016/j.tsf.2011.03.114.
[36] J.C. Pouxviel, J.P. Boilot, J.C. Beloeil, J.Y. Lallemand, NMR study of the sol/gel polymerization, J. Non Cryst. Solids 89 (1987) 345–360, http://dx.doi.org/10.1016/S0022-3093(87)80277-6.
[37] K.C. Chen, T. Tsuchiya, J.D. Mackenzie, Sol-gel processing of silica. I. The role of the starting compounds, J. Non Cryst. Solids 81 (1986) 227–237, http://dx.doi.org/10.1016/0022-3093(86)90272-3.
[38] J.C. Brinker, Hydrolysis and condensation of silicates: effects on structure, J. Non Cryst. Solids 100 (1988) 31–50.
[39] E.J.A. Pope, J.D. Mackenzie, Sol-gel processing of silica. II. The role of the catalyst, J. Non Cryst. Solids 87 (1986) 185–198, http://dx.doi.org/10.1016/S0022-3093(86)80078-3.
[40] M.A. Fardad, Catalysts and the structure of SiO2 sol-gel films, J. Mater. Sci. 35 (2000) 1835–1841, http://dx.doi.org/10.1023/A:1004749107134.
[41] J.C. Brinker, G.W. Scherer, Sol-gel Science: The Physics and Chemistry of Sol-gel Processing, London: Academic Press, San Francisco CA, 1990.
[42] R. Aelion, A. Loebel, F. Eirich, The hydrolysis and polycondensation of tetra alkoxysilanes, Recl. Des. Trav. Chim. Des. Pays-Bas. 69 (2010) 61–75, http://dx.doi.org/10.1002/recl.19500690109.
[43] R. Aelion, A. Loebel, F. Eirich, Hydrolysis of Ethyl Silicate, J. Am. Chem. Soc. 72 (1950) 5705–5712, http://dx.doi.org/10.1021/ja01168a090.
[44] D. Collina, G. Fornasari, A. Rinaldo, F. Trifirò, G. Leofanti, G. Paparatto, G. Petrini, Silica preparation via sol-gel method: a comparison with ammoximation activity, Stud. Surf. Sci. Catal. 91 (1995) 401–410, http://dx.doi.org/10.1016/S0167-2991(06)81776-3.
[45] T. Asefa, M.J. MacLachlan, N. Coombs, G.A. Ozin, Periodic mesoporous organosilicas with organic groups inside the channel walls, Nature 402 (1999) 867–871, http://dx.doi.org/10.1038/47229.
[46] J.C. Brinker, Y. Lu, A. Sellinger, H. Fan, Evaporation-induced self-assembly: nanostructures made easy, Adv. Mater. 11 (1999) 579–585, http://dx.doi.org/10.1002/(SICI)1521-4095(199905)11.
[47] D. Grosso, F. Cagnol, G.J.D.A.A. Soler-Illia, E.L. Crepaldi, H. Amenitsch, A. Brunet-Bruneau, A. Bourgeois, C. Sanchez, Fundamentals of mesostructuring through evaporation-induced self-assembly, Adv. Funct. Mater. 14 (2004) 309–322, http://dx.doi.org/10.1002/adfm.200305036.
[48] A. Schüler, D. Dutta, E. De Chambrier, C. Roecker, G. De Temmerman, P. Oelhafen, J.-L. Scartezzini, Sol-gel deposition and optical characterization of multilayered SiO2/Ti1-xSixO2 coatings on solar collector glasses, Sol. Energy Mater. Sol. Cells 90 (2006) 2894–2907.
[49] X. Wang, J. Shen, Sol-gel derived durable antireflective coating for solar glass, J. Sol-Gel Sci. Technol. 53 (2010) 322–327, http://dx.doi.org/10.1007/s10971-009-2095-y.
[50] A. Vincent, S. Babu, E. Brinley, A. Karakoti, S. Deshpande, S. Seal, Role of catalyst on refractive index tunability of porous silica antireflective coatings by sol-gel technique, J. Phys. Chem. C 111 (2007) 8291–8298, http://dx.doi.org/10.1021/jp0700736.
[51] N. Lari, S. Ahangarani, A. Shanaghi, Stable multilayer TiO2–SiO2 coatings for antireflection applications, Glas. Phys. Chem. 42 (2016) 70–77, http://dx.doi.org/10.1134/S1087659616010107.
[52] W. Theiss Hard- and Software. (n.d.). ⟨http://www.mtheiss.com/⟩.
[53] D.A.G. Bruggeman, Berechnung verschiedener physikalischer Konstanten von heterogenen Substanzen. I. Dielektrizitätskonstanten und Leitfähigkeiten der Mischkörper aus isotropen Substanzen, Ann. Phys. 24 (1935) 636–664, http://dx.doi.org/10.1002/andp.19374210205.
[54] A.L. Cauchy, Sur la réfraction et la réflexion de la lumière, Bull. Des. Sci. Math. XIV (1830) 6–10.
[55] D. Stroud, The effective media approximations: some recent developments, Super-Lattices Microstruct. 23 (1998) 567–573.
[56] C. Boissière, D. Grosso, S. Lepoutre, L. Nicole, A.B. Bruneau, C. Sanchez, Porosity and mechanical properties of mesoporous thin films assessed by environmental ellipsometric, Langmuir 21 (2005) 12362–12371.
[57] M.R. Baklanov, K.P. Mogilnikov, V.G. Polovinkin, F.N. Dultsev, Determination of pore size distribution in thin films by ellipsometric porosimetry, J. Vac. Sci. Technol. B. 18 (2000) 1385, http://dx.doi.org/10.1116/1.591390.
[58] ASTM G173-03, Standard Tables for Reference Solar Spectral Irradiances: Direct Normal and Hemispherical on 37° Tilted Surface, 2013.doi:⟨http://dx.doi.org/10.1520/G0173-03R12.2⟩.
[59] L. Scriven, Physics and Applications of dip coating and spin coating, MRS Proc. 121 (1988), http://dx.doi.org/10.1557/PROC-121-717.
[60] L.D. Landau, B.G. Levich, Dragging of a liquid by a moving plate, Acta Phisicochim. U.R.S.S. 17 (1942) 42–54.
[61] Z.A. Alothman, A review: fundamental aspects of silicate mesoporous materials, Materials 5 (2012) 2874–2902, http://dx.doi.org/10.3390/ma5122874.
[62] M. Faustini, B. Louis, P.A. Albouy, M. Kuemmel, D. Grosso, Preparation of sol-gel films by dip-coating in extreme conditions, J. Phys. Chem. C 114 (2010) 7637–7645, http://dx.doi.org/10.1021/jp9114755.
[63] M. Mizuhashi, Y. Gotoh, Glass Body Provided with an Alkali Diffusion-preventing Silicon Oxide Layer, US4485146, 1984.
[64] M. Augusto, M. Lopes, D. Jesus, G. Timò, C. Agustín-Sáenz, Anti-soiling coatings for solar cell cover glass: climate and surface properties influence, Sol. Energy Mater. Sol. Cells 185 (2018) 517–523, http://dx.doi.org/10.1016/j.solmat.2018.05.036.
[65] C. Agustin Saenz, O. Zubillaga Alcorta, M. Brizuela Parra, A Broadband Anti-reflective Sol-gel Coating Composition, Pat. Appl. EP17382016, 2017.
[66] IEC 62108 International Standard, Concentrator Photovoltaic (CPV) Modules and Assemblies - Design Qualification and Type Approval, 2016.